# High magnetic shielding properties of an MgB2 cup obtained by machining a spark-plasma-sintered bulk cylinder

# High magnetic shielding properties of an $MgB_2$ cup obtained by machining a Spark-Plasma-Sintered bulk cylinder

**Laura Gozzelino[1,2], Roberto Gerbaldo[1,2], Gianluca Ghigo[1,2], Daniele Torsello[1,2], Valentina Bonino[2,3], Marco Truccato[2,3], Mihai A Grigoroscuta[4, 5], Mihail Burdusel[4], Gheorghe V Aldica[4], Viorel Sandu[4], Iuliana Pasuk[4], and Petre Badica[4]**

[1] Department of Applied Science and Technology, Politecnico di Torino, 10129 Torino, Italy
[2] Istituto Nazionale di Fisica Nucleare, Sezione di Torino, 10125 Torino Italy
[3] Department of Physics, Interdepartmental Centre NIS, University of Torino, 10125 Torino, Italy
[4] National Institute of Materials Physics, 077125 Magurele, Ilfov, Romania
[5] University Politehnica of Bucharest, 060042 Bucharest, Romania

E-mail: laura.gozzelino@polito.it
badica2003@yahoo.com

Received xxxxxx
Accepted for publication xxxxxx
Published xxxxxx

## Abstract

Superconductors are key materials for shielding quasi-static magnetic fields. In this work, we investigated the shielding properties of an $MgB_2$ cup-shaped shield with small aspect-ratio of height/outer radius. Shape and aspect-ratio were chosen in order to address practical requirements of both high shielding factors (SFs) and space-saving solutions. To obtain large critical current densities ($J_c$), which are crucial for achieving high magnetic-mitigation performance, a high-purity starting $MgB_2$ powder was selected. Then, processing of the starting $MgB_2$ powder into high density bulks was performed by spark plasma sintering. The as-obtained material is fully machinable and was shaped into a cup-shield. Assessment of the material by scaling of the pinning force showed a non-trivial pinning behaviour. The $MgB_2$ powder selection was decisive in enlarging the range of external fields where efficient shielding occurs. The shield's properties were measured in both axial- and transverse-field configurations using Hall probes. Despite a height/outer radius aspect ratio of 2.2, shielding factors higher than $10^4$ at $T = 20$ K up to a threshold field of 1.8 T were measured in axial-field geometry at a distance of 1 mm from the closed extremity of the cup, while SFs > $10^2$ occurred in the inner half of the cup. As expected, this threshold field decreased with increased temperature, but SFs still exceeding the above mentioned values were found up to 0.35 T at 35 K. The shield's shape limits the SF values achievable in transverse-field configuration. Nevertheless, the in-field $J_c$ of the sample supported SFs over 40 at $T = 20$ K up to a field of 0.8 T, 1 mm away from the cup closure.

Keywords: magnetic shielding, $MgB_2$ bulk superconductors, machinable bulks

 

## 1. Introduction

Owing to their ability to expel magnetic flux, superconducting materials have been demonstrated to be promising candidates for the fabrication of efficient low-frequency passive magnetic shields. In particular, their use is crucial in several kinds of applications, for instance when shielding magnetic flux density over 1 T [1-3] or very low magnetic field background [4-6] is required.

Shielding properties of superconducting bulks with cylindrical and planar geometries and made from different materials have successfully been investigated [7-11]. Moreover, improvements in the shielding performance have been found by superimposing superconducting bulk and tapes [12] or taking advantage of the combined use of superconducting and ferromagnetic materials [13-15].

In this context, $MgB_2$ bulk shields have shown great potential [16-18]. Indeed, $MgB_2$ long coherence length is suitable for supporting the fabrication of large untextured polycrystalline samples, because the flow of high critical current density, $J_c$, across clean grain-boundaries is not prevented by weak-link effects, even when two pellets are joined [19]. This has fostered the development of processing techniques able to produce and assemble dense $MgB_2$ bulk samples with almost isotropic and homogeneous $J_c$, into complex geometries [17, 20-23]. The starting elements are cheap, non-toxic and do not include rare-earths, and the small weight density of this superconductor makes it attractive for portable applications such as space ones [24]. Besides this, the typical operating temperatures (20-30 K) of this compound can be easily reached using closed-cycle cryocoolers or liquid $H_2$.

All the above mentioned characteristics make $MgB_2$ able to face the major challenges in the field of magnetic shield fabrication [25]. In our previous paper [18], we reported on a novel fabrication technique that, starting from Spark Plasma Sintering (SPS) of $MgB_2$ and hexagonal BN powders, produces fully machinable $MgB_2$ bulks, which can be geometrized in order to meet specific shape requirements. The first shielding experiment carried out on a hollow cylinder, fabricated with this technique, showed promising values of the shielding factor (SF), especially considering the small aspect ratio of height/radius of the sample (1.75). In the same paper, we also demonstrated by computation how the addition of a cap (disk) on one of the tube's apertures would lead to SFs over $10^4$ at $T = 25$ K in axial applied fields up to $\mu_0 H_{appl} = 1.0$ T.

Based on these calculation results and in order to address this topic experimentally, in this work we applied the same fabrication process to produce a cup-shaped shield. With the aim of obtaining a significant improvement in the shielding factor independently from the direction of the external field, the shield was manufactured by suitably shaping a single bulk cylinder, so as to guarantee a superconducting joint between the tube and its cap. Indeed, it was demonstrated that a cap addition provides a noteworthy increase of the tube's shielding ability even in transverse-field configuration, only if cap and tube are "fused" together [26], as it happens when they are fabricated in the same process.

In addition, since high shielding performance also requires large $J_c$ values [25, 26], we worked to improve the effective current carrying cross-sectional area by an accurate selection of the starting $MgB_2$ powder.

As in our previous works [15, 18], the shielding vessel had a small aspect ratio of height/outer radius. Indeed, this geometry can be useful to address magnetic mitigation solutions in situations where the space occupied by the shield and its mass must be minimized (e.g. space applications [27, 28]). Furthermore, the choice of a small aspect ratio is necessary when the shield radius is so large that, in practice, its height cannot be much longer than the radius [29].

The paper is organized as follows. In section 2, we briefly recall the details of the sample fabrication process and describe the experimental procedures used for their characterization. The experimental results concerning X-ray diffraction analysis, the critical current density and pinning force evaluation and the shielding measurements are reported and discussed in section 3. The main findings are summarized in section 4.

## 2. Experimental details

### *2.1 $MgB_2$ fabrication process*

$MgB_2$ commercial powder was mixed with hexagonal BN (BNh, henceforth). The mixture was loaded into a graphite die with 20 mm inner diameter and processed by spark plasma sintering at 1150 °C for a dwell time of 8 min. The maximum pressure applied on the sample during sintering was 95 MPa. More details of the fabrication process are reported in [30]. The as-prepared cylinder (25 mm in height) was fully machinable [31] and, at first, it was partially bored by using drill bits and then it was refined in the final cup-shape by means of a lathe machine. Two pictures of the final

**Figure 1.** $MgB_2$ cup fabricated by spark plasma sintering, drilling and final refining on a lathe machine. Geometrical parameters: outer radius, $R_o = 10.15$ mm, inner radius, $R_i = 7.0$ mm, external height, $h_e = 22.5$ mm, internal depth, $d_i = 18.3$ mm.

product (simply named cup, henceforth) are shown in Figure 1. Its geometrical parameters are specified in the figure caption and its aspect ratio, defined as the ratio of the external height over the outer radius is 2.2.

### *2.2 Measurements details*

The structural analysis of the sample was carried out with a Bruker-AXS D8 ADVANCE diffractometer ($CuK_{\alpha 1}$ radiation, $\lambda = 1.5406$ Å). Phase concentration, crystallite size and lattice parameters of $MgB_2$ were extracted from Rietveld analysis. The bulk density of the full cylinder before shaping into cup was determined by the Archimedes method using toluene as weighting medium.

Magnetic measurements were performed with a Physical Properties Measurement System (PPMS 14 T, Quantum Design, US) on a sample with dimensions 1.5 cm × 1.5 cm × 0.5 cm cut from residual parts obtained in the shaping process of the as-Spark Plasma Sintered (as-SPSed) cylinder. Transition temperature, $T_c$, is the onset temperature of the superconducting transition in the curve of magnetization vs. temperature, $M(T)$, measured applying a magnetic field $\mu_0 H_{appl} = 10$ mT after zero-field-cooling. From magnetization loops carried out at different temperatures the critical current density, $J_c(H)$, curves were extracted by using the Bean model [32]. The irreversibility field, $H_{irr}$, obtained from the same measurements, was defined as the field at which $J_c$ is $10^2$ A/cm$^2$.

For the shielding experiment, the cup was placed in tight thermal contact with the second stage of a cryogen-free cryocooler. More details on the experimental setup are reported in Ref. 18. First, the cup was cooled in zero field down to the working temperature and then a homogenous dc field was applied either parallel or perpendicular to the sample's axis with an average rate of $1\times10^{-4}$ T/s. The local magnetic flux density was measured by means of five cryogenic Ga-As Hall probes [33] located along the cup's axis as sketched in figure 2. The probes were always oriented to measure the component of the magnetic induction parallel to the applied field (i.e. $B_z$).

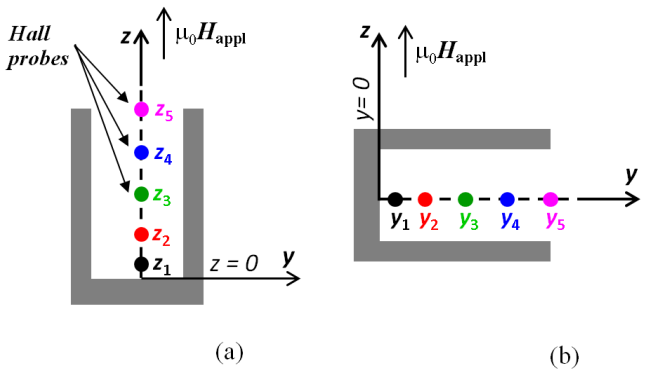


**Figure 2.** Schematic drawing of the Hall probe arrangements for the axial- (a) and transverse- (b) magnetic field measurements. In the axial-field configuration, assuming $z = 0$ the coordinate of the closed extremity, the Hall probes were positioned at $z_1 = 1$ mm, $z_2 = 5.0$ mm, $z_3 = 9.2$ mm (shield's centre) and $z_4 = 13.7$ mm and $z_5 = 18.3$ mm (shield's open extremity). Likewise, in the transverse-field configuration, assuming $y = 0$ the coordinate of the closed extremity, the Hall probes were placed at $y_1 = 1$ mm, $y_2 = 4.6$ mm, $y_3 = 9.2$ mm (shield's centre) and $y_4 = 13.7$ mm and $y_5 = 18.3$ mm (shield's open extremity). The external field was always applied parallel to $z$ axis and the Hall probes were always oriented to measure $B_z$.

## 3. Results and discussion

### *3.1 Structural analysis*

Figure 3 compares the X-ray diffraction (XRD) patterns of the starting $MgB_2$ raw powder and corresponding spark-plasma sintered sample added with BNh. In the starting powder, besides the $MgB_2$ main phase, impurity phases of MgO and Mg were present. Their weight concentration is summarized in Table 1, together with the average crystallite size. It is worth mentioning that the $MgB_2$ phase concentration in the raw powder and in the SPSed bulk was about 10 % higher than in the case of the cylinder sample investigated in Ref [18]. We also note that the ratio among secondary phases in the raw $MgB_2$ powder is much different in this work compared to the previous one [18]: for MgO it is 1.8 against 4.6 wt.%, for $MgB_4$ 0 against 7.1 wt.%, and for Mg 1.2 against 0.3 wt.%, respectively. The lower amount of non-superconducting phases, such as MgO, in the sample from this work is expected to positively affect $J_c$ since the presence of impurity phases reduces the supercurrent effective cross-section [34].

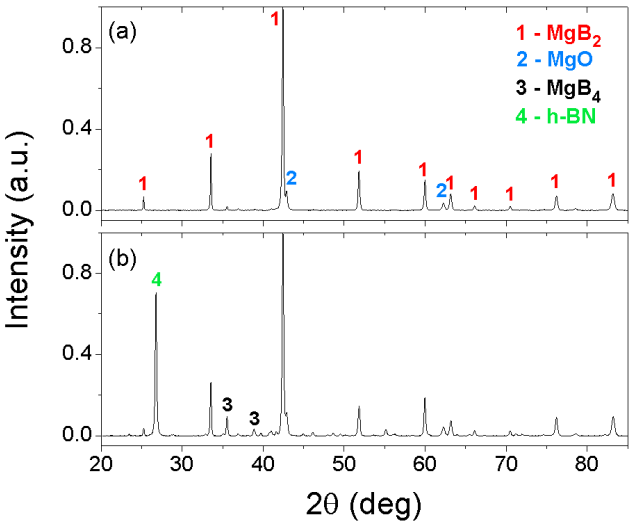


**Figure 3.** X-ray diffraction patterns of $MgB_2$ raw powder (a) and ($MgB_2$ + 10%wt BNh) sintered bulk cylinder (b).

**Table 1.** Lattice parameters, phase content (without considering the amount of BNh) and average crystallite size of the $MgB_2$ raw powder and of the final bulk product.

| | Lattice parameters [Å] | | Phase concentration [wt. %] | | | | Average crystallite size [nm] | | | |
|---|---|---|---|---|---|---|---|---|---|---|
| | a | c | $MgB_2$ | $MgB_4$ | MgO | Mg | $MgB_2$ | $MgB_4$ | MgO | Mg |
| $MgB_2$ raw powder | 3.087 | 3.522 | 97 | - | 1.8 | 1.2 | 113±10 | --- | 45±6 | 51±4 |
| $MgB_2$ bulk cylinder | 3.084 | 3.525 | 73 | 18 | 9 | - | 138±3 | 200±20 | 41±1 | - |

The density of the final bulk sample was 2.50 g/cm$^3$. Since the theoretical density of the composite is 2.62 g/cm$^3$, as determined by considering the wt.% of the component phases and their theoretical densities [30], it results a relative density of ~95%, indicating a good grain packing.

### *3.2 Critical temperature, critical current densities and pinning forces*

The normalised magnetization of the sintered bulk displays a very sharp superconducting transition, as reported in the inset of figure 4. The transition temperature is 38.9 K. This high value of $T_c$ indicates the lack of chemical reactions between $MgB_2$ and BNh powders [35]. Moreover, we argue that possible $MgB_2$ contamination with carbon from the graphite mould system during SPS processing can also be neglected since C entering on B sites strongly reduces $T_c$ [36].

The main frame of figure 4 shows the critical current density calculated from magnetic hysteresis loops as a function of the external field and for temperatures ranging from 5 to 35 K. The self-field $J_{c0}$ (figure 5(a)) reaches values of $4.0 \cdot 10^5$ and $2.7 \cdot 10^5$ A/cm$^2$ at $T = 5$ and 20 K, respectively, which are comparable or slightly higher than $J_c$ measured on undoped $MgB_2$ samples used for practical applications as bulk magnets [37, 38]. Moreover, both $J_{c0}$ and in—field $J_c$ are higher than for machinable SPSed sample from Ref [18], demonstrating the high influence of the raw $MgB_2$ powder on samples quality and performance. However, these values are lower than the highest ones for non-machinable optimally-doped SPS $MgB_2$ [39]. Indeed, the price to pay to obtain a fully machinable material, which is crucial for applications, is to have slightly lower material's performance in terms of critical current density and correlated parameters, such as the quality product ($J_{c0} \times \mu_0 H_{irr}$ - see figure 5 (b)) and the maximum pinning force, $F_{p,max}$ (figure 5 (c), being $F_p$ calculated as $\mu_0 H_{appl} \times J_c$). Conversely, the machinable sample from this work retained a high irreversibility field (figure 5(d)). Considering this observation, it is of much interest to further investigate the pinning mechanism details.

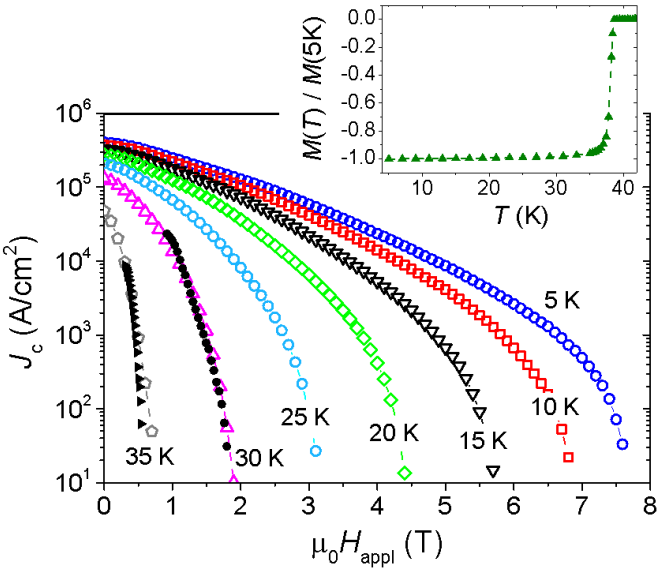


**Figure 4.** Main panel: $J_c$ dependence on the applied magnetic field at different temperatures (open symbols: $J_c$ values extracted from the hysteresis loops carried out on a small sample – see sect. 3.2; solid symbols: $J_c$ values calculated from $B_z$ vs $\mu_0 H_{appl}$ cycles measured by the Hall probe located at position $z_5$ along the cup's axis – see sect. 3.3.1). Inset: normalized magnetization of the bulk product as a function of temperature.

To this aim, the pinning forces vs. applied field curves were normalised following the universal pinning force scaling procedure reported in [40, 41]. Then, the experimental data was fitted by the law:

$$f_p = A h^p (1-h)^q \qquad (1)$$

where $f_p = F_p / F_{p,max}$, $h = H_{appl} / H_{irr}$. $A$, $p$ and $q$ are fitting parameters, and in particular, $p$, and $q$ values are correlated to vortex pinning mechanisms [41]. Moreover, considering percolation aspects and defining $h_0 = h(f_p = 1)$, the

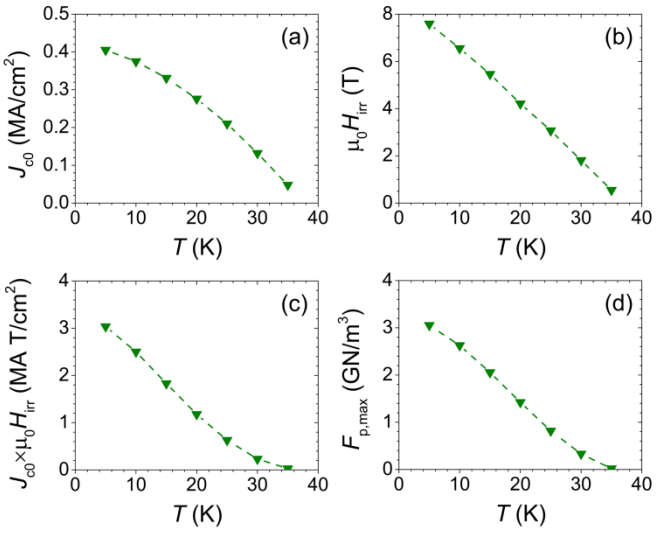


**Figure 5.** The dependencies on temperature of: (a) self-field critical current density $J_{c0}$, (b) irreversibility field $\mu_0 H_{irr}$, (c) quality product ($J_{c0} \times \mu_0 H_{irr}$), and (d) maximum pinning force $F_{p,\,max}$. Dashed lines are a guide to the eye.

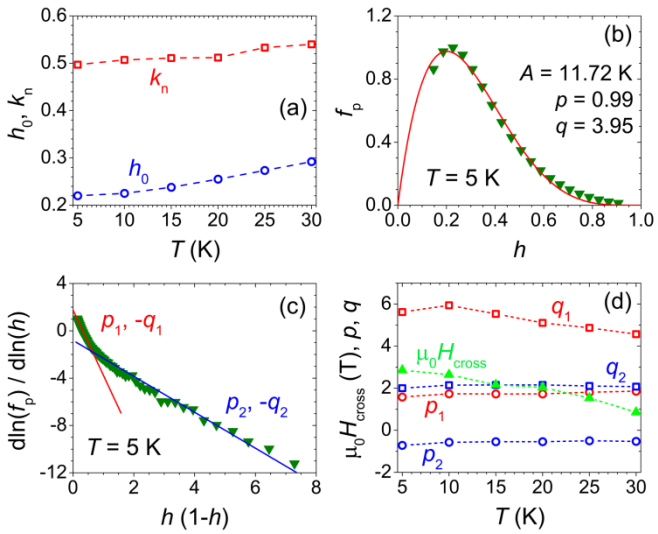


**Figure 6.** (a) Pinning force parameters $h_0$ and $k_n$ vs. temperature; (b) scaling of the pinning force at 5 K in the entire field range (continuous red line is the fit for the indicated $A$, $p$, $q$ parameters); (c) derivative of the pinning force (see text) at 5 K indicating two linear domains with linear fit parameters $p_1$, $-q_1$ and $p_2$, $-q_2$, respectively; (d) $p_1$, $q_1$, $p_2$, $q_2$ and $\mu_0 H_{cross}$ behavior with temperature. Dashed lines in figure (a) and (d) are a guide to the eye.

introduced by Eisterer [42] was also taken into account. Theoretical values for Grain-Boundary Pinning (GBP) (i.e. surface pinning) are $h_0 = 0.2$, $p = 0.5$, $q = 2$, $k_n = 0.34$ and for Point Pinning (PP) they are $h_0 = 0.33$, $p = 1$, $q = 2$, $k_n = 0.47$ [41, 42].

The parameters $h_0$, and $k_n$ are plotted as a function of temperature in figure 6(a). They show an increase with temperature and this suggests a strengthening of the point pinning at high temperatures, considering that the values $k_n$ (as well as $h_0$ at high temperatures) are close to their respective theoretical values for PP mechanism ($h_0$ = 0.33 and $k_n$ = 0.47). This is the typical case for $MgB_2$ pristine and BN added samples fabricated by SPS [39].

However, a deeper investigation in the framework of Dew-Hugues model [41] seems to indicate that different mechanisms are simultaneously active. For investigated temperatures within 5-30 K range, fits by equation (1) yielded fitting parameters that do not agree with the theory (figures 6(b),(d)). In addition, by plotting the derivative $\mathrm{d}\ln(f_p)/\mathrm{d}\ln(h)$ vs. $h/(1\text{-}h)$ two linear dependencies were obtained (figure 6(c)). The line intercept with $y$-axis and the opposite of the slope for each linear domain are the pinning force parameters $p_1$, $q_1$ and $p_2$, $q_2$, respectively. By defining $x = h/(1\text{-}h)$, the crossover coordinate between the two regions, $x_{cross}$, corresponds to the crossover scaled field $h_{cross} = \dfrac{x_{cross}}{1 + x_{cross}}$. The corresponding crossover field is $H_{cross} = h_{cross} \times H_{irr}$. Parameters $p_1$, $q_1$, $p_2$, $q_2$, and $\mu_0 H_{cross}$ are given as a function of temperature in figure 6(d). Parameters $p_1$, $p_2$, and $q_2$ almost do not depend on temperature. The exception is $q_1$ that is decreasing when temperature increases. A decrease from 2.8 to 0.8 T is also visible for $\mu_0 H_{cross}$. The values of $p_1$ (~ 1.7) and $q_1$ (4.6-5.9) and variation of the latter parameter with temperature are approximately similar to those reported in Ref. [43] for the composite non-machinable samples with starting compositions $((MgB_2)_{0.99}(Te_x(HoO_{1.5})_y)_{0.01})$, $x/y$=0.31/0.69, 0.25/0.75. On the other hand, the values of $p_2$ (~ -0.6) and $q_2$ (~ 2.1) and variation of these parameters with temperature is very different than for the indicated samples: the dependencies $p_2(T)$ and $q_2(T)$ for $MgB_2$ samples co-added with $Ho_2O_3$ and Te show a higher degree of complexity and, hence, of pinning behaviour. The physical meaning for the obtained negative values of $p_2$ from this work remains unclear and further research is needed.

### *3.3 Magnetic shielding measurements*

The shielding properties of the cup were investigated in the temperature range from 20 to 35 K. We explored the magnetic mitigation performance of the manufact in both axial- and transverse-field configuration in order to attain more meaningful information on its competitiveness in

practical applications where generic field orientations are likely.

The shielding efficiency was estimated using two parameters: the shielding factor (SF), calculated as the ratio between the applied magnetic field and the local magnetic induction measured by the Hall probes, $\mu_0 H_{appl}/B_z$, and an applied field threshold, $\mu_0 H_{appl,lim}$, above which the shielding factor drops below a given value.

### *3.3.1 Magnetic shielding in axial-field configuration*

The main frame of figure 7 provides the shielding factors evaluated at $T$ = 30 K along the cup's axis as a function of the applied field, $\mu_0 H_{appl}$, in axial-field configuration. Despite the aspect ratio of only 2.2, which makes the flux penetration from the cup's edge not negligible, SFs exceeding $10^4$ and $10^2$ was found 1 mm far from the closed extremity (position $z_1$) and in correspondence of the cup's centre (position $z_3$), respectively, up to $\mu_0 H_{appl}$ = 1.0 T. Above this field, the shielding factor sharply decreases due to a flux jump occurrence [44, 45] (figure 7, inset).

As mentioned above, we defined a threshold field, $\mu_0 H_{appl,lim||}$, as the applied field above which the shielding factor drops below a reference value, that must be different in different positions since SFs span over orders of magnitudes (see figure 7). We chose SF=$10^4$ for position $z_1$, $10^3$ for position $z_2$, and $10^2$ for position $z_3$. As expected, $\mu_0 H_{appl,lim||}$ depends on temperature, as summarized in figure

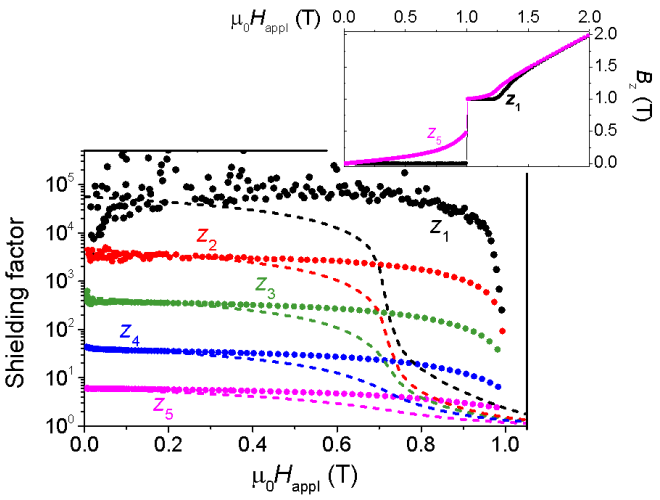


**Figure 7.** Shielding factors (symbols) measured by the five Hall probes placed along the cup's axis at $T$ = 30 K and as a function of the applied field. The dashed lines represent the shielding factors computed in correspondence of the Hall probe positions, assuming the $J_c(B)$ dependence obtained at $T$ = 30 K in [18] (see text). In the inset, the magnetic induction curves measured by the Hall probes located at positions $z_1$ and $z_5$ are plotted. At $\mu_0 H_{appl}$ = 1 T a flux-jump phenomenon clearly occurred. Measurements and computations were performed in the axial-field configuration.

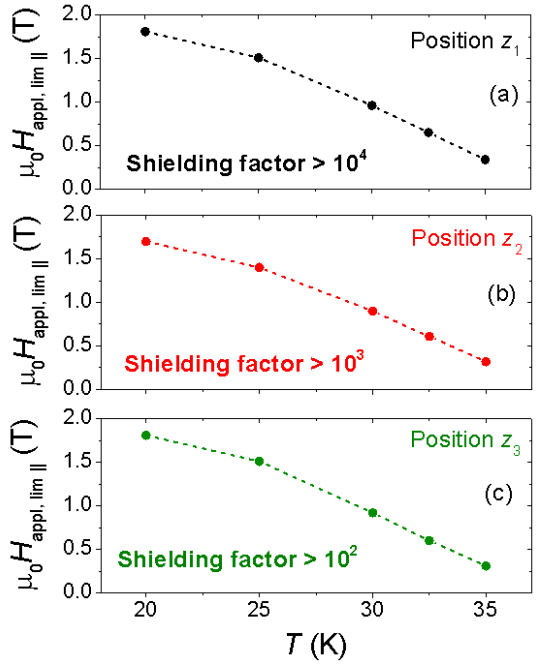


**Figure 8.** Temperature dependence of the threshold applied fields, $\mu_0 H_{appl,lim||}$, above that the shielding factor drops below $10^4$ (for position $z_1$, figure (a)), $10^3$ (for position $z_2$, figure (b)) and $10^2$ (for position $z_3$, figure (c)). Measurements were performed in the axial-field configuration and the dashed lines are a guide to the eye.

8. Remarkably, at 20 K, SF > $10^2$ up to $\mu_0 H_{appl}$ = 1.8 T were achieved in half the inner volume of the shield (figure 8 (c)). In the same range of applied fields, the SF increases over $10^4$ moving towards the closed extremity (figure 8 (a)). A further shift of $\mu_0 H_{appl,lim||}$ to higher applied field values is expected by increasing the lateral wall thickness, reducing the inner radius of the cup. In comparison, a similar SF was found at 20 K for a $YBa_2Cu_3O_7$ cup with comparable aspect ratio and lateral wall thickness, but only up to $\mu_0 H_{appl,lim||} \sim 1$ T [10].

Then, in order to investigate how the $J_c$ improvement with respect to previous samples [18] affects the shielding properties of the cup, we compared the measured SFs with those expected by assuming the same $J_c(B)$ dependence found in [18]. To this aim, we applied the numerical modelling procedure described in [18] using a cup layout with the same sizes as that characterized experimentally in this work.

As can be seen in figure 7, by assuming in SF calculation $J_c(B) = J_{c,0} \exp\left[-\left(\frac{B}{B_0}\right)^{\gamma}\right]$, where $J_{c,0}$ = 3.0 × $10^4$ A/cm$^2$, $B_0$ = 0.83 T and $\gamma$ = 2.52, i.e. the parameter values obtained in [18] at 30 K, a good agreement between experimental and computed curves is achieved only at low applied fields, where the shielding performance mainly depends on the

sample geometry. This is supported also by the evidence that in this field range the SF dependence on the distance from the closed extremity of the shield can also be described by the analytical expression calculated by Claycomb *et al.* [46, 47] for the axial field attenuation by a superconducting tube in Meissner state closed by an end cap. Following [46, 47] the expression

$$\mathrm{SF}(z_\mathrm{i})/\mathrm{SF}(z_\mathrm{j})_{|\mathrm{calc}} = \sinh\left(3.834\frac{z_\mathrm{j}}{R_\mathrm{i}}\right)\Big/\sinh\left(3.834\frac{z_\mathrm{i}}{R_\mathrm{i}}\right)$$

is predicted, being $R_\mathrm{i}$ the inner radius of the tube and $z$ the distance from the center of the end cap. Focusing on $z_2$, $z_3$ and $z_4$ positions (experimental data at $z_1$ position are too scattered), we obtained $\mathrm{SF}(z_2)/\mathrm{SF}(z_3)_{|\mathrm{calc}} = 10.0$, $\mathrm{SF}(z_3)/\mathrm{SF}(z_4)_{|\mathrm{calc}} = 11.7$ and $\mathrm{SF}(z_2)/\mathrm{SF}(z_4)_{|\mathrm{calc}} = 119$, in satisfactory agreement to the corresponding experimental ratios: 9.5, 10.0 and 94, respectively.

At higher fields, where the field-dependence of $J_\mathrm{c}$ comes into play, this analytical approach does not fit any more and the calculated curves in figure 7 clearly drop faster than the experimental ones. Considering the SF threshold values reported in figure 8, this means that the improvement of $J_\mathrm{c}$(B) raised $\mu_0 H_{\mathrm{appl,lim}||}$ of more than 0.3 T.

Finally, we checked if the critical current density measured on a small sample and reported in figure 4 (open symbols) can be considered representative of the actual current flowing in the whole cup. To address this topic, we measured again the magnetic induction at $T$ = 30 and 35 K by the Hall probes positioned along the cup's axis. To minimize the flux jump occurrence, we furtherly decreased the ramp rate of the applied field down to $5\times10^{-5}$ T/s. Then, we calculated $J_c$ from the $B_z$ vs $\mu_0 H_{\mathrm{appl}}$ cycle measured by the Hall probe located at position $z_5$ (i.e. in correspondence to the cup's open extremity) as proposed by Bartolomé *et al.* for finite superconducting rings [48]:

$$J_c = \frac{\Delta B_c}{\mu_0\ \mathrm{f}(R_o, R_i, d_i, z)} \qquad (2)$$

where $\Delta B_c = B_\mathrm{c}^+ - B_\mathrm{c}^-$ is the induction cycle width measured at a given applied field in the axial-field configuration and the function f provides the dependency of $J_c$ on the geometry of the system:

$$\mathrm{f}(R_o, R_i, d_i, z) = \left(\frac{d_i}{2} - z\right)\ln\left(\frac{R_o + \sqrt{R_o^2 + (z - d_i/2)^2}}{R_i + \sqrt{R_i^2 + (z - d_i/2)^2}}\right) +$$

$$+\left(\frac{d_i}{2} + z\right)\ln\left(\frac{R_o + \sqrt{R_o^2 + (z + d_i/2)^2}}{R_i + \sqrt{R_i^2 + (z + d_i/2)^2}}\right)$$

In our case $R_o$ and $R_i$ are the outer and inner radii of the cup, respectively, $d_i$ the cup internal depth and $z$ the distance from the cup's centre (i.e $z = z_3$). We used the $B_z$ data measured by the Hall probe located at $z_5$, since in that position the effects of the cup closure can be disregarded [18]. Notably, focusing on high field region, i.e. above the full penetration field in the first-magnetization curve of the cup, where the Bean model is expected to give realistic $J_\mathrm{c}$ values [49], the agreement is good (figure 4). Comparisons at lower temperatures could not be carried out because of the multiple occurrences of flux jumps that prevented the $J_c$ evaluation using the Hall probes.

### *3.3.2 Magnetic shielding in transverse-field configuration*

The main frame of figure 9 presents the SFs evaluated along the cup's axis at $T$ = 30 K and as a function of the applied field as in figure 7, but in transverse-field configuration. The shielding ability of the cup is much lower than for the axial-field configuration even at low applied fields, as expected for this geometry [29].

Likewise in the axial-field configuration, in the low field range the shielding performance mainly depends on the sample shape. Indeed, the SF dependence on the distance from the closed extremity is still suitably described by the analytical expression calculated in [46, 47] for the transverse field attenuation by a superconducting cup in Meissner state:

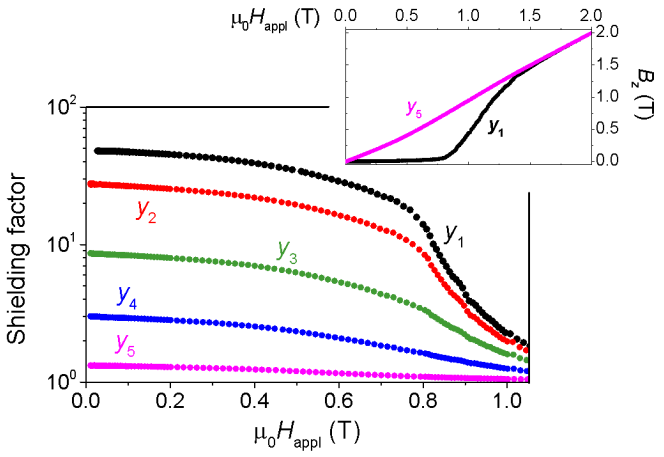


**Figure 9.** Shielding factors (symbols) measured in the transverse-field configuration by the five Hall probes placed along the cup's axis at $T$ = 30 K. In the inset, the magnetic induction curves measured by the Hall probes located at positions $y_1$ and $y_5$ are plotted.

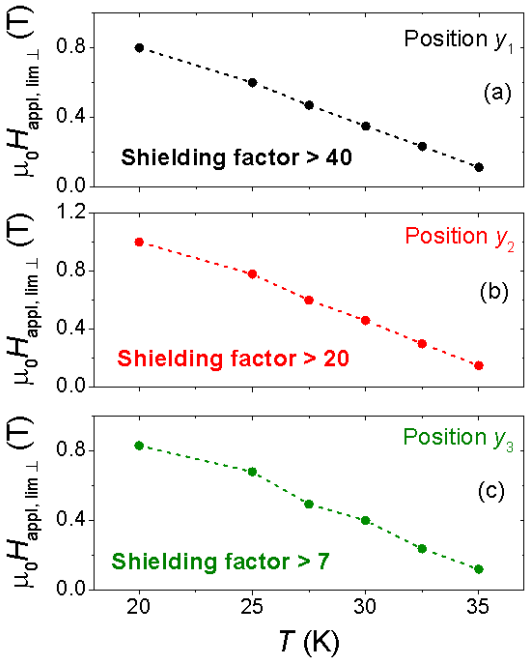


**Figure 10.** Temperature dependence of the threshold applied fields, $\mu_0 H_{appl,lim}$, above that the shielding factor drops below 40 (for position $y_1$, figure (a)), 20 (for position $y_2$, figure (b)) and 7 (for position $y_3$, figure (c)). Measurements were performed in the transverse-field configuration and the dashed lines are a guide to the eye.

$$SF(y_i)/SF(y_j)_{|calc} = \cosh\left(1.84\frac{y_j}{R_i}\right)\Big/\cosh\left(1.84\frac{y_i}{R_i}\right)$$

being $y$ the distance from the center of the closure cap.

Fixing on $y_2$, $y_3$ and $y_4$ positions, we obtained $SF(y_2)/SF(y_3)_{|calc}$ = 3.1, $SF(y_3)/SF(y_4)_{|calc}$ = 3.2 and $SF(y_2)/SF(y_4)_{|calc}$ = 10.0, in well agreement to the corresponding experimental ratios: 3.2, 2.9 and 9.1, respectively.

On the other hand, the large values of in-field $J_c$ guarantee a smooth decrease or even a flat behaviour of the SF vs. $\mu_0 H_{appl}$ curves up to high applied fields.

As we did in the axial-field configuration, we defined three threshold fields, $\mu_0 H_{appl,lim\perp}$, as the applied field above that the shielding factor goes below 40 (for position $y_1$), 20 (for position $y_2$) and 7 (for position $y_3$). In figure 10, $\mu_0 H_{appl,lim\perp}$ values are plotted as a function of temperature. As can be seen, near to the cup's closed edge (position $y_1$), at 20 K SF is over 40 up to $\mu_0 H_{appl}$ = 0.8 T, while in the same field range it is over 7 in correspondence to the cup's centre (position $y_3$).

## 5. Conclusions

With the aim of obtaining a superconducting magnetic shield with small height/ lateral dimension aspect ratio and significant SFs for different orientations of the external field, we fabricated an $MgB_2$ cup-shaped shield via mechanical machining of an $MgB_2$ bulk cylinder produced by spark plasma sintering of BNh-added $MgB_2$ powder.

Large $J_c$ values, which are essential for reaching a high magnetic-shielding capability, were obtained by a careful selection of the starting powder operated by X-ray diffraction analysis. $J_c$ homogeneity was also proved by the agreement between the values measured on a small sample cut from machining residual parts and those obtained from the whole cup characterization. However, no clear indication on a prevalent pinning mechanism was given by the analysis of the pinning forces, but different mechanisms seem to be simultaneously active.

Shielding properties of the cup-shaped shield was investigated in both axial- and transverse-field geometries as a function of temperature, applied magnetic field and Hall-probe position along the sample's axis. Despite a height/external-radius aspect ratio of only 2.2, in the axial-field configuration, inside the cup and 1 mm away from its closed extremity, we measured SFs exceeding $10^4$ at $T$ = 20 K up to $\mu_0 H_{appl}$ = 1.8 T. Moreover, in the same temperature and field region, SFs > $10^2$ still persisted in the whole inner half of the cup. In addition, the range of external fields where such efficient shielding occurred is much larger than that expected on the basis of the modelling approach and related parameters reported in [18]. This result proves the high influence of the quality of the raw $MgB_2$ powder on shield performance.

Although the transverse-field geometry intrinsically limits the shield performance [29], the in-field $J_c$ of the sample allowed SFs over 40 to be still measured at $T$ = 20 K up to $\mu_0 H_{appl}$ = 0.8 T at a distance of 1 mm from the cup closure.

Further improvements in the shielding performance are expected by further enhancing the critical current density or by superimposing additional superconducting [29] or ferromagnetic [21, 50, 51] layers. On the other hand, an increase of $J_c$ could favour flux-jump occurrence, limiting the practical applications of $MgB_2$ shields. Thus, minimizing this phenomenon, without compromising $J_c$ values and shielding performance, is the next challenging goal in this research field.

## Acknowledgements

V. B. and M. T. acknowledge partial support from the "Departments of Excellence" (L. 232/2016) grant, funded by the Italian Ministry of Education, University and Research (MIUR), and from the project BIOMB (Reference Number 4114) funded by the consortium M-ERA.NET. Romanian

team gratefully acknowledges UESFISCDI, projects POC 37_697 No. 28/01.09.2016 REBMAT, ERA-M 74/2017 BIOMB (Reference Number 4114), and Core Program PN19-03 (contract no. 21 N/08.02.2019).

## References


[1] Pourrahimi S, Williams J, Punchard W, Tuttle J, DiPirro M, Canavan E and Shirron P 2008 *Cryogenics* **48** 253-7
[2] Barna D 2017 *Phys. Rev. Accel. Beams* **20** 041002
[3] Barna D, Giunchi G, Novák M, BrunnerK, Német A, Petronez C, Atanasovz M, Bajasz H and Feuvrierz J 2019 *IEEE Trans. Appl. Supercond., in press,* DOI: 10.1109/TASC.2019.2920359
[4] Seki Y, Kandori A, Suzuki D and Ohnuma M 2005 *Appl. Phys. Lett.* **86** 243902
[5] Giunchi G, Bassani E, Cavallin T, Bancone N and Pavese F 2007 *Supercond. Sci. Technol.* **20** L39–41
[6] Bergen A, van Weers H J, Bruineman C, Dhallé M M J, Krooshoop H J G, ter Brake H J M, Ravensberg K, Jackson B D and Wafelbakker C K 2016 *Rev. Sci. Instrum.* 87 105109
[7] Denis S, Dusoulier L, Dirickx M, Vanderbemden P, Cloots R, Ausloos M and Vanderheyden B 2007 *Supercond. Sci.Technol.* **20** 192–201
[8] Terao Y, Sekino M, Ohsaki H, Teshima H and Morita M 2011 *IEEE Trans. Appl. Supercond.* **21** 1584-7
[9] Fagnard J-F, Elschner S, Bock J, Dirickx M, Vanderheyden B and Vanderbemden P 2010 *Supercond. Sci. Technol.* **23** 095012
[10] Wéra L, Fagnard J -F, Namburi D K, Shi Y, Vanderheyden B and Vanderbemden P 2017 *IEEE Trans. Appl. Supercond.* **27** 6800305
[11] Yang P, Fagnard J F, Vanderbemden P and Yang W *Supercond. Sci. Technol* 2019 *Supercond. Sci. Technol.* **32** 115015
[12] Tomków Ł. Ciszek M and Chorowski M 2015 *J. Appl. Phys.* **117** 043901
[13] Gömöry F, Solovyov M, Šouc J, Navau C, Prat-Camps J and Sanchez A 2012 *Science* **335** 1466–8
[14] Prat-Camps J, Navau C and Sanchez A 2015 *Sci. Rep.* **5** 12488
[15] Gozzelino L, Agostino A, Gerbaldo R, Ghigo G and Laviano F 2012 *Supercond. Sci. Technol.* **25** 115013
[16] Rabbers J J, Oomen M P, Bassani E, Ripamonti G and Giunchi G 2010 *Supercond. Sci. Technol.* **23** 125003
[17] Giunchi G, Barna D, Bajas H , Brunner K, Nèmet A and Petrone C 2018 *IEEE Trans. Appl. Supercond.* **28** 6801705
[18] Gozzelino L, Gerbaldo R, Ghigo G, Laviano F, Torsello D, Bonino V, Truccato M, Batalu D, Grigoroscuta M A, Burdusel M, Aldica G V and Badica P 2019 *Supercond. Sci. Technol.* **32** 034004
[19] Mikheenko P, Yurchenko V V and Johansen T H 2012 *Supercond. Sci. Technol.* **25** 045009
[20] Giunchi G, Ripamonti G, Cavallin T and Bassani E 2006 *Cryogenics* **46** 237-40
[21] Gozzelino L, Gerbaldo R, Ghigo G, Laviano F, Truccato M and Agostino A 2016 *Supercond. Sci. Technol.* **29**, 034004
[22] Agliolo Gallitto A, Camarda P, Li Vigni M, Figini Albisetti A, Saglietti L and Giunchi G 2014 *IEEE Trans. Appl. Supercond.* **24** 1500109
[23] Bhagurkar A G, Yamamoto A, Hari Babu N, Durrell J H, Dennis A R and Cardwell D A 2015 *Supercond. Sci. Technol.* **28** 015012
[24] Giunchi G, Ripamonti G, Cavallin T, Bassani E, 2006 *Cryogenics* **46** 237-42
[25] Durrell J H, Ainslie M D, Zhou D, Vanderbemden P, Bradshaw T, Speller S, Filipenko M and Cardwell D A 2018 *Supercond. Sci. Technol.* **31** 103501
[26] Wéra L, Fagnard J-F, Hogan K, Vanderheyden B, Namburi D K, Shi Y, Cardwell D A and Vanderbemden P 2019 *IEEE Trans. Appl. Supercond.* **29** 6801109
[27] Giunchi G 2014 *Proc. of the 20th IMEKO TC4 Symp. On Measurements of Electrical Quantities* (Budapest: IMEKO) pp 1020–4
[28] Prouvé T, Duval J M, Luchiera N and D'escrivan S, 2014 *Cryogenics* **64** 201-6
[29] Fagnard J F, Vanderheyden B, Pardo E and Vanderbemden P 2019 *Supercond. Sci. Technol.* **32** 074007
[30] Aldica G, Batalu D, Popa S, Ivan I, Nita P, Sakka Y, Vasylkiv O, Miu L, Pasuk I and Badica P, 2012 *Physica C* **477** 43-50.
[31] Aldica G, Burdusel M, Cioca V and Badica P Patent No RO130252-A2, DPAN 2015-383635
[32] Bean C P 1962 *Phys. Rev. Lett.* **8** 250–3
[33] Gozzelino L, Minetti B, Gerbaldo R, Ghigo G, Laviano F, Agostino A and Mezzetti E 2011 *IEEE Trans. Appl. Supercond.* **21** 3146-9
[34] Li W and Dou S-X, 2015 in "*Superconductors: New Developments*" (ed. by Alexander Gabovich, IntechOpen) pp. 95-126 (Available from: https://www.intechopen.com/books/superconductors-new-developments/high-critical-current-density-mgb2)
[35] Badica P, Aldica G, Burdusel M, Popa S, Negrea RF, Enculescu M, Pasuk I and Miu L 2014 *Supercond. Sci. Technol.* **27** 095013
[36] Mickelson W, Cumings J, Han W Q and Zettl A 2002 *Phys. Rev. B* **65** 052505
[37] Bhagurkar A G, Yamamoto A, Wang L, Xia M, Dennis A R, Durrell J H, Aljohani T A, Babu N H and Cardwell D A 2018 *Sci. Rep.* **8** 13320
[38] Fujishiro H, Naito T and Yoshida T 2014 *Supercond. Sci. Technol.* **27** 065019
[39] Badica P, Aldica G, Ionescu A M, Burdusel M and Batalu D 2017 in "*Correlated Functional Oxides: Nanocomposites and Heterostructures*" (ed. by H. Nishikawa et al., Springer International Publishing AG) pp. 75-116
[40] Fietz W A and Webb W W 1969 *Phys. Rev. B* 178 657-67
[41] Dew-Hughes D 1974 *Philos. Mag.* **30** 293–305
[42] Eisterer M 2008 *Phys. Rev. B* **77** 144524
[43] Badica P, Aldica G, Burdusel M, Grigoroscuta M, Ionescu A M, Sandu V, Popa M, Euculescu M, Pasuk I, Kuncser A, 2020 in "*Superconductivity from materials science to practical applications*" (ed. by P. Mele et al., Springer Nature Switzerland AG) pp. 303-24
[44] Romero-Salazar C, Morales F, Escudero R, Durán A and Hernández-Flores O A 2007 *Phys. Rev. B* **76** 104521
[45] Ghigo G,Gerbaldo R, Gozzelino L, Laviano F, Lopardo G, Monticone E, Portesi C and Mezzetti E 2009 *Appl. Phys. Lett.* **94** 052505
[46] Claycomb J R and Miller J H 1999 *Rev Sci Instrum* **70** 4562-8
[47] Claycomb J R 2016 in "Applied Superconductivity - Handbook on Devices and Applications", edited by P Seidel, (Weinheim:Wiley-VCH Verlag GmbH & Co. KGaA) pp. 780-806
[48] Bartolomé E, Granados X, Palau A, Puig T, Obradors X, Navau C, Pardo E, Sánchez A and Claus H 2005 *Phys. Rev. B* **72** 024523

[49] Chen D -X and Goldfarb R B 1989 *J. Appl. Phys.* **66** 2489-500
[50] Omura A, Oka M, Mori K and Itoh M 2003 *Physica C* **386** 506–11
[51] Gozzelino L, Gerbaldo R, Ghigo G, Laviano F, Truccato M 2017 *J Supercond Nov Magn* **30** 749-56